JCI The Journal of Clinical Investigation

5-HT orchestrates Histone Serotonylation and Citrullination to Drive Neutrophil Extracellular Traps and Liver Metastasis

Kaiyuan Liu, … , Kai Zhang, Helen He Zhu

J Clin Invest. 2025. https://doi.org/10.1172/JCI183544.

Research In-Press Preview Cell biology Oncology

Graphical abstract

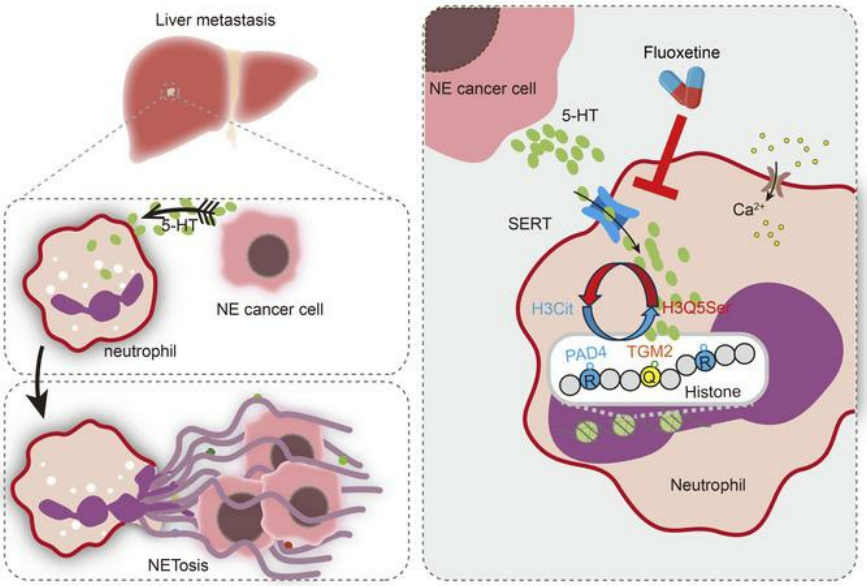

5-HT orchestrates Histone Serotonylation and Citrullination to Drive Neutrophil Extracellular Traps and Liver Metastasis

Authors: Kaiyuan Liu[1#], Yingchao Zhang[1#], Genyu Du[1], Xinyu Chen[1], Lingling Xiao[2], Luyao Jiang[1], Na Jing[1], Penghui Xu[3], Chaoxian Zhao[1], Yiyun Liu[1], Huifang Zhao[1], Yujiao Sun[1], Jinming Wang[1], Chaping Cheng[1], Deng Wang[3], Jiahua Pan[1], Wei Xue[1], Pengcheng Zhang[4], Zhi-Gang Zhang[1], Wei-Qiang Gao[1,3], Shu-Heng Jiang[1], Kai Zhang[1*], and Helen He Zhu[1*]

Affiliations:

[1]State Key Laboratory of Systems Medicine for Cancer, Renji-Med-X Stem Cell Research Center, Department of Urology, Renji Hospital, Shanghai Cancer Institute, Shanghai Jiao Tong University School of Medicine, Shanghai, China;

[2]Department of Emergency Medicine, Shanghai Seventh People's Hospital, Seventh People's Hospital of Shanghai University of Traditional Chinese Medicine, Shanghai, China;

[3]Med-X Research Institute, School of Biomedical Engineering, Shanghai Jiao Tong University, Shanghai, China;

[4]School of Biomedical Engineering, Shanghai Tech University, Shanghai, China.

[#] These two authors contribute equally to this paper.

Correspondence*: Helen He Zhu (zhuhecrane@shsmu.edu.cn), and Kai Zhang (zhangkaishida@126.com), Tel: 86-21-62932049, Fax: 86-21-68383916.

Address: Renji Hospital, 160 Pujian Rd., Shanghai, 200127, China.

Abstract

Serotonin (5-HT) is a neurotransmitter that has been linked to tumorigenesis. Whether and how 5-HT modulates cells in the microenvironment to regulate tumor metastasis remains to be largely unknown. Here, we demonstrate that 5-HT is secreted by neuroendocrine prostate cancer (NEPC) cells to communicate with neutrophils and to induce neutrophil extracellular traps (NETs) in the liver, which in turn facilitates the recruitment of disseminated cancer cells and promotes liver metastasis. 5-HT induces histone serotonylation (H3Q5ser) and orchestrates histone citrullination (H3cit) in neutrophils to trigger chromatin decondensation and facilitate the formation of NETs. Interestingly, we uncover in this process a reciprocally reinforcing effect between H3Q5ser and H3cit and a crosstalk between the respective writers TGM2 and PAD4. Genetic ablation or pharmacological targeting of TGM2, or inhibiting 5-HT transporter (SERT) with the FDA-approved antidepressant drug fluoxetine reduces H3Q5ser and H3cit modifications, suppresses NETs formation, and effectively inhibits NEPC, small cell lung cancer, and thyroid medullary cancer liver metastasis. Collectively, the 5-HT-triggered NETs production highlights a targetable neurotransmitter-immune axis in driving liver metastasis of neuroendocrine cancers.

Introduction

Apart from the classical role of neurotransmitters in neuronal activity, they have long been implicated in the pathological process of different tumor types (1). Serotonin (5-HT) is a neurotransmitter that is positively involved in cancer development by promoting cancer cell proliferation and invasion (2-4). The precise manner in which 5-HT modulates the tumor microenvironment to regulate metastasis remains largely unknown. Recently, it has been reported that 5-HT can be taken up into cells via the serotonin transporter (SERT) and be covalently added to the glutamine residue of target proteins such as small guanosine triphosphate hydrolases (GTPase) and glyceraldehyde-3-phosphate dehydrogenase (GAPDH) by the enzyme transglutaminase 2 (TGM2) to regulate platelet granule release and $CD8^+$ T cell activity, respectively (5-7). Whether 5-HT plays a role in innate immune cells from the tumor microenvironment to regulate cancer progression remains to be elucidated.

Neutrophils are the most abundant cell type in innate immunity. In response to pathogen invasion, neutrophil formed neutrophil extracellular traps (NETs), web-like structures composed of decondensed chromatin and antimicrobial proteins, to kill pathogens (8). Intriguingly, recent studies in cancers suggested that NETs act to promote metastasis by attracting circulating tumor cells or activating dormant cancer cells. Neutrophil chromatin decondensation is a required process for NETs formation (9-11). Serotonylation in the 5^{th} glutamine residue of histone H3 (H3Q5ser) has been recently found to participate in chromatin dynamics regulation to activate a permissive transcriptional state (6). Therefore, we hypothesized that 5-HT and H3Q5ser may play a role in NETs formation. Crosstalk among different histone modifications has been recently demonstrated to be essential in the intricate regulation of chromatin dynamics (12). Histone citrullination (H3cit) catalyzed by PAD4 is reported to be critical for

chromatin decondensation in NETs (13). Whether H3cit interacts with other histone modification such as H3Q5ser in the process of NETs formation is an interesting but unexplored question.

Metastasis is the major cause of death in prostate cancer (PCa) (14, 15). Accumulating evidence shows that the liver, a severely understudied target organ in PCa, is frequently colonized by advanced PCa, especially by the most lethal neuroendocrine prostate cancer (NEPC) variant with a rate of more than 45% (16, 17). These patients with liver metastases had the worst median overall survival (18). We have previously generated a murine NEPC orthotopic implantation model with a high penetrance of liver metastasis (19). Accumulation of neutrophils in the liver of this NEPC tumor-bearing mouse model was interestingly found at early stage of liver metastasis (19). NEPC displays features of neuroendocrine cells including the production of neuroactive peptides and neurotransmitters such as 5-HT (2, 20, 21). We asked whether disseminated NEPC communicates with neutrophils in the liver via 5-HT to shape a metastasis-favorable microenvironment.

Here, we identified that 5-HT induces TGM2-mediated H3Q5ser and enhances PAD4-catalyzed H3cit to drive NETs formation. NEPC-derived 5-HT promotes the prostate-to-liver metastasis by crosstalk with hepatic neutrophils.

Results

Neutrophil infiltration and NETs formation at early stage promote NEPC liver metastasis.

To investigate how immune microenvironment regulates metastasis in the liver, we analyzed immune cell profile in NEPC liver metastasis via a multi-omics-based computational tool, Multi-omics Immuno-Oncology Biological Research (IOBR), on a previously reported Stand-Up-to-Cancer (SU2C) dataset (22-24). As shown in Figure 1A, neutrophils were the most abundant immune cells in liver metastasis of PCa patients. We then compared the neutrophil enrichment among different PCa metastatic sites using the SU2C dataset, and found a predominant neutrophil infiltration in liver metastasis compared to metastatic lesions in other distant sites (Figure 1B). We previously developed a NEPC liver metastasis mouse model, in which, the *PbCre*$^{+}$;*Rb1*$^{f/f}$;*Trp53*$^{f/f}$ (*Rb1*$^{\Delta/\Delta}$*Trp53*$^{\Delta/\Delta}$) tumor organoid was inoculated into the prostate of wild type (WT) C57BL/6 mice (19). Consistently, flow cytometric analysis on this model revealed that Cd11b^{+}Ly6G^{+} neutrophils accumulated in livers with micro-metastases less than 200 μm in diameter, suggesting an increase of neutrophils at the early stage of liver metastasis (Figures 1, C and D).

The production of neutrophil extracellular traps (NETs) is an important function of neutrophils. We performed immunohistochemical (IHC) staining against a well-established neuroendocrine differentiation marker, the neural cell adhesion molecule-1 (Ncam1), and conducted immunofluorescence (IF) co-staining against myeloperoxidase (MPO), a neutrophil marker, and histone H3 citrullination (H3cit), a NETs marker, on serial sections of normal WT liver and liver metastases from the *Rb1*$^{\Delta/\Delta}$*Trp53*$^{\Delta/\Delta}$ organoid-implanted mice (Figure 1E). Quantification of H3cit and MPO double positive cell frequency showed significantly increased NETs formation from

126 micro to macro liver metastases of *Rb1*$^{\Delta/\Delta}$*Trp53*$^{\Delta/\Delta}$ NEPC tumor-bearing mice in
127 contrast to normal liver samples from WT mice (Figure 1F).

128 Next, we determined the NETs formation in both primary prostate tumors and liver
129 metastases in NEPC patients. As shown in Supplemental Figure 1, A and B, CD66^{+}
130 neutrophil-derived NETs (H3cit^{+}) were much more enriched in liver metastases
131 compared to primary sites. To determine whether hepatic NETs contributed to NEPC
132 metastasis, we injected DNase I to digest NETs in *Rb1*$^{\Delta/\Delta}$*Trp53*$^{\Delta/\Delta}$ NEPC tumor-bearing
133 mice. Treatment of DNase I degraded NETs formation (Figure 1, G and H.), and
134 significantly reduced number of liver metastatic foci (Figure 1, I and J.). Notably,
135 DNase I treatment significantly prolonged the survival of *Rb1*$^{\Delta/\Delta}$*Trp53*$^{\Delta/\Delta}$ NEPC tumor-
136 bearing mice compared to vehicle control (Figure 1K). Next, we investigated the impact
137 of NETs on the attraction and retention of NEPC cells. To do this, the bone marrow-
138 derived neutrophils (BMDNs) were isolated from WT C57BL/6 mice, and stimulated
139 with the NETs inducer, phorbol 12-myristate 12-acetate (PMA). Compared to the
140 vehicle control, NETs formed from PMA-stimulated murine BMDNs significantly
141 enhanced the migration (Figure 1L) and adhesion (Figure 1M) of *Rb1*$^{\Delta/\Delta}$*Trp53*$^{\Delta/\Delta}$ NEPC
142 cells. Collectively, these data suggest that recruitment of neutrophils and NETs
143 formation promote the liver metastasis in NEPC.

144

145 **5-HT secreted from NEPC potentiates NETs formation and NEPC liver metastasis.**

146 5-HT is a well-characterized neurotransmitter, produced by brain serotonergic
147 neurons, enterochromaffin cells and neuroendocrine tumors (25). Several lines of
148 evidence have shown that neuroendocrine cancer cells, such as NEPC, produce high
149 levels of 5-HT (21, 25). In support of this, we analyzed the RNA-seq data of the
150 Beltran's prostate cancer dataset(26), and found that the 5-HT biosynthesis enzyme

Tryptophan Hydroxylase 1 (TPH1) was markedly upregulated in NEPC compared to other PCa subtypes (Supplemental Figure 1C). These findings led us to explore whether NEPC-secreted 5-HT can affect NETs formation and NEPC liver metastasis.

To this end, we treated murine BMDNs with 5-HT, and used a potent inducer of NETs, the PMA, as a positive control (27). The cell-impermeant dye SytoxGreen, which can bind to DNA released by neutrophils, was stained and imaged to serve as a measurement of NETs. We found that the number of NETs formed by 5-HT-stimulated neutrophils was similar to that induced by PMA (Figure 2, A and B). We next collected the conditioned-medium (CM) from scramble shRNA (scram-CM) and sh*Tph1*-infected (sh*Tph1*-CM) $Rb1^{\Delta/\Delta}Trp53^{\Delta/\Delta}$ NEPC organoids in which 5-HT production was blocked to stimulate murine BMDNs respectively (Supplemental Figure 1, D and E). In contrast to scram-CM, sh*Tph1*-CM incurred less NETs production, as evidenced by the reduced percentages of SytoxGreen^{+} cells (Figure 2, C and D) and H3cit^{+} neutrophils (Supplemental Figure 1, F and G). To confirm whether these results were applicable to the human context, we purified human peripheral blood-derived neutrophils (PBDNs) and observed increased NETs formation of human PBDNs in response to 5-HT stimulation (Figure 2, E and F, and Supplemental Figure 1, H and I). NET-DNAs have a decondensed structure compared to intact chromatin DNAs, making them more susceptible to digestion into smaller fragments by micrococcal nuclease (MNase) (11). HL-60 cells can be induced to differentiate into granulocytes by N, N-Dimethylformamide (DMF). Upon calcium ionophore treatment, HL-60-derived granulocytes release long stretches of decondensed chromatin and form NETs (11). We therefore conducted MNase digestion assay on HL-60 granulocytes and found that addition of 5-HT accelerated the process of MNase-mediated DNA digestion compared to the calcium ionophore treatment alone (Figure 2G). These data indicate that 5-HT

derived from NEPC can induce the formation of NETs.

For *in vivo* experiments, the scramble and sh*Tph1*-transfected $Rb1^{\Delta/\Delta}Trp53^{\Delta/\Delta}$ NEPC organoids were intravenously inoculated into WT C57BL/6 mice. A significantly reduced liver metastatic burden was observed in the mice receiving the *Tph1* knockdown (*Tph1*-KD) organoids (Figures 2, H-J.). On the other hand, the attenuated liver metastasis induced by *Tph1*-KD NEPC organoids was reversed upon 5-HT reconstitution (Figure 2, H-J.), suggesting the crucial role of 5-HT in promoting NEPC liver metastasis. Co-IF staining of H3cit and MPO revealed that *Tph1*-KD in NEPC organoids led to suppressed hepatic NETs formation in nearby areas of metastatic cancer cells compared to scramble shRNA-transfected counterparts (Figure 2K-L). Interestingly, the attenuated NETs formation ($H3cit^{+}MPO^{+}$ signal) induced by *Tph1*-KD organoids was restored by 5-HT reconstitution *in vivo* (Figure 2, K and L).

To test whether 5-HT is also important for liver metastasis in other neuroendocrine cancer types, we conducted *in vivo* experiments using the human small cell lung cancer (SCLC) NCI-H82 cells (Supplemental Figure 2, A-E.) and the human medullary thyroid cancer TT cells (Supplemental Figure 2, F-J.). Consistent with the data from the NEPC liver metastasis model, *TPH1*-KD in either NCI-H82 cells or TT cells resulted in significantly suppressed liver metastasis (Supplemental Figure 2, A-C. and 2, F-H.) and decreased NETs formation (Supplemental Figure 2, D and E and 2, I and J) in both NCI-H82 and TT xenograft models. Collectively, *Tph1*-mediated 5-HT synthesis plays an important role in promoting the liver metastasis of pleiotropic neuroendocrine malignancies, including NEPC, SCLC, and medullary thyroid cancer, via facilitating NETs formation.

TGM2-mediated H3Q5ser promotes NETs formation.

5-HT could either activate 5-HT receptors (HTR) or be transported into the cell through the serotonin transporter (SERT) (Figure 3A). When transported into the nucleus, 5-HT can covalently bind to histone catalyzed by transglutaminase 2 (TGM2), leading to histone H3Q5ser modification (Figure 3A). This modification has recently been shown to increase chromatin accessibility (28). Therefore, we asked whether H3Q5ser modulates chromatin status in neutrophils and participates in NETs formation. To this end, murine BMDNs were induced for NETs production by 5-HT, or PMA as a positive control. IF staining for H3Q5ser, SytoxGreen and H3cit were conducted to evaluate H3Q5ser levels and NETs formation. The results showed that 5-HT treatment led to an increase in positive H3Q5ser signals with a concomitant increment of NETs formation and H3cit levels in murine BMDNs (Figure 3, B-G.) and human PBDNs (Supplemental Figure 3A). Next, the SERT inhibitor fluoxetine (Fluox) and the TGM2 inhibitor LDN-27219 (LDN) were used to block either 5-HT intake or H3Q5ser modification in neutrophils (Figure 3A). IF staining data suggested that 5-HT-promoted H3Q5ser modification in murine BMDNs was inhibited by either Fluox or LDN (Figure 3, B and C). In line with the decreased H3Q5ser levels, we also detected an evident attenuation of NETs formation, as exemplified by reductions in SytoxGreen (Figure 3, D and E) and H3cit (Figure 3, F and G) signals in response to either Fluox or LDN treatment. We then tested whether TGM2 facilitates NET-DNA decondensation. The MNase Digestion Assay revealed that suppression of TGM2 resulted in a MNase hyposensitivity profile, which was indicative of a less open chromatin architecture (Figure 3H). Next, we isolated murine BMDNs from a *Tgm2* knockout (*Tgm2*$^{-/-}$) mice. Immunoblotting data revealed a concomitant decrease in H3Q5ser and H3cit modifications upon the genetic ablation of *Tgm2* (Supplemental Figure 3B). Compared to WT murine BMDNs, IF staining images showed that 5-HT-induced NETs formation

was significantly suppressed in *Tgm2*$^{-/-}$ murine BMDNs (Figure 3, I-K.). These data suggest a critical role of TGM2 in chromatin decondensation and NETs formation.

In addition to the 5-HT/SERT signaling, 5-HT can also bind and activate its corresponding receptor (5-HT receptor, HTR) to initiate downstream signaling cascades (Figure 3A). We therefore asked whether the 5-HT/HTR signaling is also involved in H3Q5ser modification and/or NETs formation as well. According to previous literature, HTR1B has been reported to highly expressed in neutrophils (29). We also re-analyzed Beltran's clinical prostate cancer bulk RNA-seq data of NEPC liver metastasis (26), and found that the HTR1B was the highest HTR at mRNA level in NEPC liver metastatic biospecimens (Supplemental Figure 4A). We therefore blocked HTR1B activity in murine neutrophils using HTR1B inhibitor SB224289 (Figure 3A), and found that 5-HT-induced H3Q5ser modification (H3Q5ser^{+} signal) and NETs formation (SytoxGreen^{+} and H3cit^{+} signals) were not significantly affected upon HTR1B inhibition (Supplemental Figure 4, B-E.).

To further corroborate the essential role of H3Q5ser on NETs formation (Figure 4A), we overexpressed either HA-tagged histone H3.3-WT or H3.3-Q5A mutant in HL-60 granulocytes (Figure 4B). As shown in Figure 4B, Q5A mutation of H3.3 blocked the formation of H3Q5ser. Meanwhile, the H3cit deposition was markedly attenuated when H3Q5ser was inactivated. IF results further showed that NETs formation was significantly suppressed when the H3Q5ser modification was inhibited in the H3.3(Q5A) expressing HL-60 cells in comparison to H3.3(WT)-transfected counterparts (Figure 4, C-F.). Furthermore, the MNase assay results demonstrated a less accessible chromatin structure in H3.3(Q5A)-transfected HL-60 cells as compared to that in H3.3(WT)-transfected cells (Figure 4G). Altogether, these results demonstrated that TGM2-mediated H3Q5ser facilitates NETs formation.

Genetic deletion or small molecule inhibition of TGM2 suppresses NEPC liver metastasis.

We subsequently investigated the impact of TGM2 inhibition on NEPC liver metastasis. Syngeneic C57BL/6 mice were injected intravenously with *Rb1*$^{\Delta/\Delta}$*Trp53*$^{\Delta/\Delta}$ NEPC organoids. TGM2 inhibitor LDN (Figure 3A) was applied starting from 4 days post inoculation. We noticed a significant reduction of liver metastasis in LDN-treated mice (Figure 5, A-D.). IF staining on liver sections of vehicle and LDN-treated NEPC tumor-bearing mice revealed a significant decrease in H3Q5ser modifications in hepatic neutrophils upon LDN (Figure 5, E and F). In accordance with repressed H3Q5ser levels, H3cit modification in hepatic neutrophils was simultaneously suppressed (Figure 5, G and H). To validate the role of TGM2 in driving liver metastasis in other neuroendocrine cancer types, we treated the SCLC NCI-H82 cell-inoculated nude mice with the TGM2 inhibitor LDN. As shown in Supplemental Figure 5, A-C, significantly attenuated liver metastatic lesions were observed in LDN-treated SCLC tumor-bearing mice compared to vehicle-treated counterparts. Co-IF staining of H3Q5ser/MPO and H3cit/MPO revealed a significant reduction of H3Q5ser levels (Supplemental Figure 5, D and E) and NETs production (Supplemental Figure 5, F and G) in liver sections upon LDN treatment *in vivo*.

On the other hand, we employed the WT and *Tgm2*$^{-/-}$ mice as xenograft recipients for *Rb1*$^{\Delta/\Delta}$*Trp53*$^{\Delta/\Delta}$ NEPC organoids. Significant reductions in liver metastasis foci (Supplemental Figure 6, A and B), NETs formation (Supplemental Figure 6, C and D) and H3Q5ser deposition (Supplemental Figure 6, E and F) were observed in *Tgm2* knockout recipient mice. Therefore, our data demonstrate a crucial role of TGM2 in NEPC metastasis in the liver.

TGM2 collaborates with PAD4 to orchestrate histone serotonylation and citrullination.

It is very interesting that H3Q5ser and H3cit display the same trend of change during the formation of NETs, in response to treatment of H3Q5ser inhibitor, or upon introduction of histone 3 mutations (Figure 3, B-G., Figure 4, B-F., and Figure 5, E-H.). These findings, together with the approximate locations of these two modifications on the histone 3 backbone (Figure 6A), led us to explore the potential crosstalk between H3Q5ser and H3cit during NETs formation.

Next, we assessed the impact of inhibition or knockdown of respective catalytic enzymes on these two histone modifications by immunoblotting. Consistent with IF staining data in Figure 2, A and B and E and F, addition of 5-HT markedly promoted the deposition of H3Q5ser and H3cit in HL-60 granulocytes (Figure 6B). Strikingly, inhibition of TGM2 by LDN led to a marked downregulation of both H3Q5ser and H3cit in HL-60 granulocytes (Figure 6B). Addition of fluoxetine resulted in a simultaneous inhibition of H3Q5ser and H3cit (Figure 6B). On the other hand, treatment of PAD4 inhibitor Cl-amidine also caused prominent decreases in H3cit and H3Q5ser (Figure 6B). To validate this finding, we knocked down PAD4 or TGM2 in HL-60 granulocytes and found that downregulation of PAD4 or TGM2 results in prominent reductions of both modifications (Figure 6C). Moreover, the MNase digestion assay showed that either TGM2 (Figure 6D) or PAD4 (Figure 6E) knockdown suppressed the decondensed chromatin state that is required for NETs formation. Therefore, these data suggested a mutually enhanced effect between TGM2-catalyzed H3Q5ser and PAD4-mediated H3cit.

Furthermore, we used an alternative human cell line, HEK-293T cells, which

barely express TGM2 and PAD4, as a clean system to conduct exogenous expression of HA-tagged TGM2 and FLAG-tagged PAD4 (6, 30). As shown in Figure 6F, we found that co-expression of PAD4 and TGM2 in HEK-293T led to a synergistic effect in promoting deposition of both H3cit and H3Q5ser. In addition, we introduced enzyme dead mutant of TGM2(C277S) or PAD4(C645S) into HEK-293T cells. A reduction of H3cit was detected when TGM2 was inactively mutated (Figure 6G). Meanwhile, we found that PAD4 inactivated mutation led to a H3Q5ser suppression (Figure 6G). Those data together with the immunostaining results in Figure 2 and 3 indicated that H3Q5ser and H3cit are closely linked histone modifications.

To decipher the underlying mechanism of H3Q5ser and H3cit crosstalk, we first tested whether an interaction exists between their respective enzyme PAD4 and TGM2. We performed immunoprecipitations of exogenous PAD4 and TGM2 in HEK-293T cells. As shown in Figure 6, H and I, we detected a physical association of PAD4 and TGM2 by co-immunoprecipitation (co-IP). The protein interaction of endogenous PAD4 and TGM2 was also detected in HL-60 cells (Supplemental Figure 7, A and B). To further decipher the physical association between PAD4 and TGM2, we subcloned truncated mutations of these two proteins based on their well-characterized protein domains (Supplemental Figure 7, C and D). Co-IP results revealed that the first immunoglobulin-like domain (D1) of PAD4 and the third carboxy-terminal barrel domain (D3) of TGM2 were required for their physical interaction (Supplemental Figure 7, E and F). Moreover, we noticed that 5-HT addition further enhanced the binding between PAD4 and TGM2 (Supplemental Figure 7, G and H). Additionally, we performed pull-down assay using purified PAD4 and TGM2 proteins and demonstrated a direct physical binding between these two enzymes (Figures 6, J and K). Together, these data revealed a functional interplay between PAD4 and TGM2 that acts to

orchestrate histone serotonylation and citrullination.

H3Q5ser and H3cit are mutually permissive modifications.

To directly examine the putative role of H3Q5ser on H3cit modification, we transduced either H3.3(WT) or H3.3(Q5A) into HEK-293T cells. As expected, the mutation of the 5th glutamine residue of H3.3 to alanine residue prevented serotonylation on H3 (Figure 6A and Figure 7A). This downregulation of histone serotonylation led to a reduction of H3cit level (Figure 7A). In addition, we generated the R2A, R8A, R17A and R2, 8, 17A combinatorial mutations of H3 to eliminate citrullination at these sites (Figure 6A). As shown in Figure 7B, transfection of these mutations decreased the H3cit mark in concordance with a reduced H3Q5ser deposition. We investigated whether the H3.3(Q5A) or H3.3(R2,8,17A) mutant, which blocks H3Q5ser or H3cit modification, affects the recruitment of each other's epigenetic writer. Interestingly, H3.3(Q5A) mutation impeded the binding of both PAD4 and TGM2 to H3 (Figure 7C). Similarly, we detected a deficient recruitment of both PAD4 and TGM2 to histone when the H3.3(R2,8,17A) mutant was introduced (Figure 7D). These data suggest that H3cit and H3Q5ser are mutually permissive histone modifications.

A recent study reported that PAD2, another PAD family enzyme, promotes PCa progression and castration resistance via Histone H3 citrullination at the 26th arginine (R26) residue (H3R26cit)(31)(Figure 6A). We asked whether PAD2-mediated H3R26cit affects the modulation of H3Q5ser and NETs formation. A PAD2 inhibitor, AFM-30a (AFM), was used to treat murine BMDNs in the presence of 5-HT. PAD2 inhibition did not significantly affect 5-HT-induced NETs production (Supplemental Figure 8, A and B). To further assess the putative role of H3R26cit in H3Q5ser modification, we transfected HEK-293T cells with H3.3(WT) or H3.3(R26A)

constructs. As shown in Supplemental Figure 8C, the mutation of H3.3(R26A) did not affect H3Q5ser modification. Moreover, co-IP results revealed that PAD2 was not physically associated with TGM2 (Supplemental Figure 8, D and E). These results suggest that PAD2-catalyzed H3R26cit is not involved in H3Q5ser modification and NETs formation.

To directly analyze the effect of H3Q5ser modification on the addition of H3cit mark and *vice versa*, we performed *in vitro* histone serotonylation or citrullination assays. *In vitro* catalytic reaction using purified PAD4 on H3 and H3Q5ser peptides showed that serotonylation on H3Q5 substantially enhanced the PAD4-mediated H3cit deposition compared to unmodified H3 (Figure 7, E and F). Concordantly, citrullination on H3 also strengthened the TGM2-mediated H3Q5ser signal compared to unmodified H3 (Figure 7, G and H). These results further support a mutual promoting effect between the formation of H3cit and H3Q5ser modifications.

To determine the relationship between H3Q5ser and H3cit chromatin occupancy, we conducted CUT & Tag experiments and compared the anti-H3cit and anti-H3Q5ser antibody immunoprecipitated DNA sequence. As shown in Figure 7, I-L., genome-wide localization analysis on HL-60 cells revealed a substantial overlap between H3Q5ser-occupied and H3cit-marked genomic regions. Notably, NETs formation-related genes, including *ITGB2*, *DNASE1*, *ITGAM*, *RIPK1*, *MPO,* and *AKT1,* were detected in the H3Q5ser and H3cit co-occupied gene locus (Figure 7M). Together, our results suggest that TGM2-catalyzed H3Q5ser and PAD4-mediated H3cit are closely linked and share a substantial overlap of regulatory genomic regions on a genome-wide scale.

Targeting SERT by fluoxetine blocks liver metastasis of NE cancers

To investigate the clinical application of our findings, we applied FDA-approved

SERT inhibitor fluoxetine (Fluox) into *Rb1*$^{\Delta/\Delta}$*Trp53*$^{\Delta/\Delta}$ NEPC organoids intravenously injected C57BL/6 mice. As shown in Figure 8, A-C., treatment with fluoxetine effectively inhibited liver metastasis burden (Figure 8A). Mice that received fluoxetine therapy displayed significant reductions in liver weight (Figure 8B) and number of metastases (Figure 8C). Both H3Q5ser and H3cit staining intensities were decreased in fluoxetine-treated liver metastatic lesions, suggesting that inhibition of 5-HT uptake suppressed H3Q5ser (Figure 8, D and E). MPO and H3cit co-stained NETs were significantly less presented in the liver metastasis sections of fluoxetine-treated group (Figure 8, F and G). To further explore whether these findings identified in NEPC were also applied to other neuroendocrine cancers, we performed additional experiments using the SCLC NCI-H82 cells (Supplemental Figure 9) and medullary thyroid cancer TT cells (Figure 8, H-N.). In line with the results of NEPC mouse model, fluoxetine treatment significantly repressed NCI-H82 (Supplemental Figure 9, A-C.) and TT (Figure 8, H-J.) liver metastasis *in vivo*. IF staining images demonstrated concomitant reductions in both H3Q5ser and H3cit in MPO^{+} neutrophils in metastasis containing liver sections in SCLC (Supplemental Figure 9, D-G.) and medullary thyroid (Figure 8, K-N.) cancer models. These data supported a potential therapeutical value of the Food and Drug Administration (FDA)-approved SERT inhibitor fluoxetine in blocking NETs formation and preventing liver metastasis of pleiotropic NE cancers.

Discussion

Here we demonstrate that 5-HT, derived from neuroendocrine cancer cells, promotes liver metastasis through a crosstalk with neutrophils. 5-HT is taken up by accumulating neutrophils in the liver via SERT and induces TGM2-mediated histone serotonylation. In concert with PAD4-catalyzed histone citrullination, histone serotonylation leads to a decondensed chromatin status in neutrophils, triggering NETs formation, also named as NETosis. NETs then recruit and trap cancer cells, leading to cancer metastasis (Supplemental Figure 10, Graphical abstract). Therapeutically, inhibition of 5-HT intake via the SERT inhibitor fluoxetine can effectively abrogate liver metastasis in preclinical mouse models (Supplemental Figure 10, Graphical abstract). Therefore, in addition to the well-known role of 5-HT in nervous system, our findings show that the neurotransmitter 5-HT acts as a positive regulator in facilitating a pro-metastatic microenvironment in neuroendocrine cancers.

We elucidate the mechanism by which epigenetic modification of histone serotonylation is required to promote NETs formation in a 5-HT-dependent manner. Serotonylation has been implicated in different substrate proteins with biological functions. Our recent work reported that serotonylation of GAPDH promotes $CD8^+$ T cell activation (7). In the current study, we uncover a function of 5-HT-induced and TGM2-catalyzed histone seronotylation in neutrophil, a subtype of innate immune cells. This conclusion is supported by multiple lines of evidence including TGM2 or SERT inhibition, TGM2 mutation or knockout, and H3 (Q5A) mutation. We include three NE-cancer models, NEPC, SCLC and thyroid medullary cancer in this study. Of note, central nervous system cancers such as glioblastoma or nerve-infiltrating cancers also produce high levels of 5-HT (32, 33). Whether a similar mechanism of 5-HT-induced histone serotonylation in neutrophils and NETs formation is also involved in the

progression of these malignancies would be interesting to explore.

We uncover a reciprocally reinforcing effect between the histone modifications of H3Q5ser and H3cit, and a previously unreported crosstalk between their respective writers of TGM2 and PAD4. Coordinated histone modifications have been demonstrated to be essential for regulating chromatin accessibility and transcriptional activity (12). For example, it has been shown that Nsd1-mediated H3K36me2 co-localizes with PRC2-mediated H3K27me2 and that histone methyltransferase Nsd1 modulates the Polycomb repressive complex 2 (PRC2) function to demarcate H3K27me2 and H3K27me3 for transcriptional regulation (34, 35). In the current study, another collaboration between H3Q5ser and H3cit is revealed, based on exquisite biochemical experiments including TGM2 and PAD4 knockdown or enzymatically dead mutations, the H3Q5ser (H3Q5A) and H3cit (H3R2,8,17A) deficient mutation, as well as the immunoprecipitation, pull-down, CUT&Tag-seq, and *in vitro* histone serotonylation and citrullination assays using multiple cell lines in both murine and human settings. Furthermore, using *Tgm2* knockout mice and orthotopically and intravenously inoculated preclinical models of NEPC, SCLC and thyroid medullary cancer, our results imply that the crosstalk between H3Q5ser and H3cit is of functional importance in NETs formation and cancer metastasis. Given that H3Q5ser plays a vital role in neuronal differentiation and olfactory sensory processing, and that PAD4-expressing neurons release citrullinated proteins in Alzheimer's disease, the crosstalk between H3Q5ser and H3cit may also be relevant to nervous system functions and awaits future study (6, 36, 37).

In summary, we find that histone serotonylation and histone citrullination are two closely linked types of histone modifications in neutrophils that are orchestrated to regulate chromatin decondensation, drive NETs formation, and promote liver

metastasis. 5-HT-driven NETs production highlights a targetable neurotransmitter-immune axis in driving liver metastasis of neuroendocrine cancers. Targeting the key enzyme of 5-HT biosynthesis enzyme Tph1, serotonylation enzyme TGM2 or 5-HT transporter SERT are found to effectively inhibit the NETs formation and liver metastasis in NEPC. Among them, the SERT inhibitor fluoxetine is an FDA-approved antidepressant drug with good biosafety and bioavailability (2), suggesting a promising translational value in drug repurposing. Interestingly, a recent study showed that fluoxetine inhibits NEPC growth by suppressing the cell-autonomous role of 5-HT on cancer cells (38). Different from this related work, our study focuses mainly on NEPC liver metastasis and demonstrates that fluoxetine blocks H3Q5ser and NETs formation by interfering with the effects of 5-HT on neutrophils. Therefore, fluoxetine acts as a potential drug in harnessing cancer cell growth and distant metastasis of advanced prostate cancer via different mechanisms.

Not only limited to NEPC, a high incidence of liver metastasis is commonly seen in pleiotropic neuroendocrine malignancies (33, 39, 40). In addition to the three kinds of tested NE cancer models including NEPC, SCLC, and medullary thyroid cancer in this study, the molecular mechanism and therapeutic strategy we propose is informative for a wide range of NE malignancies with such a propensity for liver metastasis.

Methods

Sex as a biological variable.

Our study on prostate cancer used male mice, as it is a male-exclusive disease. For experiments on small cell lung cancer and medullary thyroid cancer, male mice were chosen due to their lower phenotypic variability. The relevance of these findings to female mice is unknown.

Mice.

All animals used in this study were housed under humidity and temperature-controlled condition with a regular light-and-dark cycle in the specific pathogen-free facilitates at Renji Hospital. The prostate-specific dual-depletion of *Rb1* and *Trp53* transgenic mouse model *Probasin-Cre*$^{+}$; *Rb1*$^{f/f}$; *Trp53*$^{f/f}$ (*Rb1*$^{\Delta/\Delta}$*Trp53*$^{\Delta/\Delta}$) mice were obtained from the Jackson laboratory. The conventional *Tgm2*-knockout (*Tgm2*$^{-/-}$) mice were commercially available from Cyagen Biosciences Co. Ltd (Jiangsu, China). The 6~8-week-old C57BL/6 mice and athymic nu/nu nude mice were purchased from Shanghai SLAC laboratory animal Co.Ltd (Shanghai, China).

Cell lines.

The human granulocyte cell line HL-60 cells, human small cell lung cancer cell line NCI-H82 cells, medullary thyroid carcinoma cell line TT cells, and HEK-293T cells were purchased from Cell Bank of Chinese Academy of Sciences (Shanghai, China). The *Rb1*$^{\Delta/\Delta}$*Trp53*$^{\Delta/\Delta}$ NEPC murine prostate cancer organoids were established and cultured as previously reported (19). All cells used in this study have been validated

by short tandem repeat (STR) analyses. The cells were maintained in incubators at 37°C with 5% CO_2. HL-60 cells were cultured in IMDM (Gibco) with 20% FBS. NCI-H82 cells were cultured in RPMI-1640 (Gibco) with 10% FBS. TT and HEK-293T cells were cultured in DMEM (Gibco) with 10% FBS.

Immune analysis.

In detail, the Stand Up to Cancer (SU2C) prostate cancer dataset was downloaded and the gene expression matrix of liver metastases was obtained. Next, we employed the quanTIseq function in Multi-omics Immuno-Oncology Biological Research (IOBR) R package (https://github.com/IOBR/IOBR, version: 4.3.2) to analyze the infiltration of immune cells in liver metastatic biospecimens from 6 patients (n = 6). The enrichment of 10 immune cell subsets in liver metastasis was generated by the quanTIseq function. Subsequently, the ggplot function in the ggplot2 (3.5.1) package was used to generate a pie chart revealing fractions of the 10 subsets of infiltrating immune cells, including B cell, dentritic cell (DC), M1-macrophage (mac-M1), M2-macrophage (mac-M2), monocyte (mono), Neutrophils (Neutro), Natural killer cell (NK), $CD4^+$, and $CD8^+$ T cells, and regulatory T cell in Figure 1A. In addition, the frequencies of neutrophil in adrenal, bone, liver, lymph node, and other visceral metastatic sites were analyzed using the quanTIseq function to generate a violin plot (vioplot R package 0.5.0) in Figure 1B.

Tumor xenograft experiments.

The wild type (WT) C57BL/6 mice (6~8-week-old) were intravenously injected with 2,000 *Rb1*$^{\Delta/\Delta}$*Trp53*$^{\Delta/\Delta}$ organoid spheres. For DNase I treatment, mice were intraperitoneally injected (i.p.) with DNase I at the dosage of 50 μg per mouse every other day, starting from day 4 after inoculation, until the mice were sacrificed on day 30. For LDN-27219 treatment, mice were i.p. injected daily with 15 mg/kg LDN-27219 from day 4 after inoculation, and maintain the daily administration until day 30. For the fluoxetine treatment, 10 mg/kg of fluoxetine was administered via oral gavage every other day from day 4 after inoculation until the mice were sacrificed on day 30. The nude mice (6-week-old, male) were intravenously injected with 5×10^5 human TT cells or 5×10^5 human NCI-H82 cells. Nude mice were i.p. injected with 15 mg/kg LDN-27219 every other day, starting from day 4 after inoculation until day 30 when the tumor-bearing mice were sacrificed. 10 mg/kg of fluoxetine per mouse was administrated to the *Rb1*$^{\Delta/\Delta}$*Trp53*$^{\Delta/\Delta}$ organoid-inoculated mice via oral gavage from day 4 to day 30 after inoculation. Fluoxetine was dissolved in drinking water at a concentration of 20 mg/L.

***In vitro* NETs production assay.**

To assess NETs formation, coverslips were put into 24-well plates in advance, and neutrophils were seeded in RPMI-1640 or conditioned medium (CM) at the number of 2.5×10^5 cells per well. 5-HT (100 μM), TGM2 inhibitor (LDN-27219, 10 μM), SERT inhibitor (fluoxetine, 10 μM), PAD4 inhibitor (Cl-amidine, 100 μM) or CM were added to stimulate neutrophils for 12 to 16 h. The SytoxGreen (Beyotime, C1070M) and

Hoechst (Invitrogen, H3570) staining were performed immediately after these stimulated neutrophils were collected. Anti-H3cit, anti-H3Q5ser, and anti-MPO immunostainings were performed after cells were fixed with 4% paraformaldehyde (PFA). Images were captured using the Confocal Microscopy Cell Observer (ZEISS). The number of $H3cit^+$, $H3Q5ser^+$ and MPO^+ cells were quantified using the Image-J software.

Statistics.

Data were statistically analyzed using the GraphPad 8.4.3 software. Data were presented as mean ± SEM. Kaplan-Meier analysis was performed to analyze animal survival, and Log-rank test was used for comparison among groups. The correlation between 2 modification levels was analyzed via Spearman's correlation test. Two-tailed student's *t*-tests or Mann-Whitney tests were used to determine the significance in two-group experiments. One-way ANOVA tests or Kruskal-Wallis tests were used to determine the significance in multiple group experiments. Data with statistical significance (* $P < 0.05$; ** $P < 0.01$; *** $P < 0.001$) or with no statistical significance (ns) were indicated in the figure panels.

Study approval.

All animal experiments were approved by the Animal Use and Care Committee at Renji Hospital, Shanghai Jiao Tong University School of Medicine. The collection and utilization of patient clinical samples including primary prostate tumors and liver metastases were approved by the Ethics Committee of Renji Hospital, Shanghai Jiao

Tong University School of Medicine. Informed consents were obtained from patients and donors.

Data availability.

The CUT&Tag data in this study have been deposited into the database of the China National Center for Bioinformation with the accession number HRA007336. Values of all data points are presented in the Supporting Data Values file. Other methods were available in **Supplemental Methods and Materials**.

Author contributions

K.Y.L and Y.C.Z performed most of the experiments and contributed equally to this work. G.Y.D, X.Y.C and C.X.Z conducted bioinformatic analyses and CUT&Tag experiments. L.L.X and N.J assisted in data collection and biochemical assays. P.H.X, H.F.Z, J.M.W, C.P.C and D.W helped with cell culture and plasmid construction. Y.Y.L, L.Y.J and Y.J.S assisted in mice breeding. W.X and J.H.P provided clinical samples. W-Q.G, Z-G.Z, S-H.J and P.C.Z provide important discussion, technical help and assisted in manuscript preparation. H.H.Z, K.Z and K.Y.L wrote the manuscript. H.H.Z and K.Z were funded. H.H.Z and K.Z supervised this study. H.H.Z conceived this study.

Declaration of interests

The authors declare no conflict of interests.

Acknowledgements

The study was supported by funds from the National Natural Science Foundation

of China (U23A20454, 82372873) , Shanghai Pilot Program for Basic Research-Shanghai Jiao Tong University (21TQ1400225), Collaborative Innovation Center for Clinical and Translational Science by Ministry of Education & Shanghai (CCTS-202402), the Shanghai Municipal Education Commission-Gaofeng Clinical Medicine Grant Support (20181706), the Innovative research team of high-level local universities in Shanghai, and the 111 project (B21024), and RJZH25-005 from Ren Ji Hospital to H.H.Z. This study was also supported by National Natural Science Foundation (82472909), RJTJ24-MS-026 of Ren Ji Hospital, and Open Project funding KF2413 from the State Key Laboratory of System Medicine for Cancer to K.Z. We thank the staff at the integrated laser microscopy center and flow cytometry core of National Facility for Protein Science in Shanghai.

615 **References**

616 1. Jiang SH, Hu LP, Wang X, Li J, and Zhang ZG. Neurotransmitters: emerging
617 targets in cancer. *Oncogene.* 2020;39(3):503-15.

618 2. Schneider MA, Heeb L, Beffinger MM, Pantelyushin S, Linecker M, Roth L, et
619 al. Attenuation of peripheral serotonin inhibits tumor growth and enhances
620 immune checkpoint blockade therapy in murine tumor models. *Science*
621 *translational medicine.* 2021;13(611):eabc8188.

622 3. Peters MA, Walenkamp AM, Kema IP, Meijer C, de Vries EG, and Oosting SF.
623 Dopamine and serotonin regulate tumor behavior by affecting angiogenesis.
624 *Drug resistance updates : reviews and commentaries in antimicrobial and*
625 *anticancer chemotherapy.* 2014;17(4-6):96-104.

626 4. Slominski RM, Raman C, Chen JY, and Slominski AT. How cancer hijacks the
627 body's homeostasis through the neuroendocrine system. *Trends in*
628 *neurosciences.* 2023;46(4):263-75.

629 5. Walther DJ, Peter JU, Winter S, Höltje M, Paulmann N, Grohmann M, et al.
630 Serotonylation of small GTPases is a signal transduction pathway that triggers
631 platelet alpha-granule release. *Cell.* 2003;115(7):851-62.

632 6. Farrelly LA, Thompson RE, Zhao S, Lepack AE, Lyu Y, Bhanu NV, et al.
633 Histone serotonylation is a permissive modification that enhances TFIID
634 binding to H3K4me3. *Nature.* 2019;567(7749):535-9.

635 7. Wang X, Fu SQ, Yuan X, Yu F, Ji Q, Tang HW, et al. A GAPDH serotonylation
636 system couples CD8(+) T cell glycolytic metabolism to antitumor immunity.

637 *Molecular cell.* 2024;84(4):760-75 e7.

638 8. Brinkmann V, Reichard U, Goosmann C, Fauler B, Uhlemann Y, Weiss DS, et
639 al. Neutrophil extracellular traps kill bacteria. *Science (New York, NY).*
640 2004;303(5663):1532-5.

641 9. Yang L, Liu Q, Zhang X, Liu X, Zhou B, Chen J, et al. DNA of neutrophil
642 extracellular traps promotes cancer metastasis via CCDC25. *Nature.*
643 2020;583(7814):133-8.

644 10. Albrengues J, Shields MA, Ng D, Park CG, Ambrico A, Poindexter ME, et al.
645 Neutrophil extracellular traps produced during inflammation awaken dormant
646 cancer cells in mice. *Science.* 2018;361(6409).

647 11. Wang Y, Li M, Stadler S, Correll S, Li P, Wang D, et al. Histone
648 hypercitrullination mediates chromatin decondensation and neutrophil
649 extracellular trap formation. *Journal of Cell Biology.* 2009;184(2):205-13.

650 12. Valencia-Sánchez MI, De Ioannes P, Wang M, Truong DM, Lee R, Armache JP,
651 et al. Regulation of the Dot1 histone H3K79 methyltransferase by histone
652 H4K16 acetylation. *Science (New York, NY).* 2021;371(6527).

653 13. Wang Y, Li M, Stadler S, Correll S, Li P, Wang D, et al. Histone
654 hypercitrullination mediates chromatin decondensation and neutrophil
655 extracellular trap formation. *J Cell Biol.* 2009;184(2):205-13.

656 14. Thiery-Vuillemin A, Poulsen MH, Lagneau E, Ploussard G, Birtle A, Dourthe
657 LM, et al. Impact of Abiraterone Acetate plus Prednisone or Enzalutamide on
658 Patient-reported Outcomes in Patients with Metastatic Castration-resistant

659 Prostate Cancer: Final 12-mo Analysis from the Observational AQUARiUS
660 Study. *Eur Urol.* 2020;77(3):380-7.
661 15. Siegel RL, Miller KD, and Jemal A. Cancer statistics, 2020. *CA: a cancer*
662 *journal for clinicians.* 2020;70(1):7-30.
663 16. Pezaro C, Omlin A, Lorente D, Rodrigues DN, Ferraldeschi R, Bianchini D, et
664 al. Visceral disease in castration-resistant prostate cancer. *European urology.*
665 2014;65(2):270-3.
666 17. Vargas Ahumada J, González Rueda SD, Sinisterra Solís FA, Pitalúa Cortés Q,
667 Torres Agredo LP, Miguel JR, et al. Multitarget Molecular Imaging in
668 Metastatic Castration Resistant Adenocarcinoma Prostate Cancer with Therapy
669 Induced Neuroendocrine Differentiation. *Diagnostics (Basel, Switzerland).*
670 2022;12(6).
671 18. Pond GR, Sonpavde G, de Wit R, Eisenberger MA, Tannock IF, and Armstrong
672 AJ. The prognostic importance of metastatic site in men with metastatic
673 castration-resistant prostate cancer. *European urology.* 2014;65(1):3-6.
674 19. Liu K, Jing N, Wang D, Xu P, Wang J, Chen X, et al. A novel mouse model for
675 liver metastasis of prostate cancer reveals dynamic tumour-immune cell
676 communication. *Cell proliferation.* 2021;54(7):e13056.
677 20. Balakrishna P, George S, Hatoum H, and Mukherjee S. Serotonin Pathway in
678 Cancer. *International journal of molecular sciences.* 2021;22(3).
679 21. Hansson J, and Abrahamsson PA. Neuroendocrine pathogenesis in
680 adenocarcinoma of the prostate. *Annals of oncology : official journal of the*

European Society for Medical Oncology. 2001;12 Suppl 2:S145-52.

22. Zeng D, Ye Z, Shen R, Yu G, Wu J, Xiong Y, et al. IOBR: Multi-Omics Immuno-Oncology Biological Research to Decode Tumor Microenvironment and Signatures. *Frontiers in immunology.* 2021;12:687975.

23. Robinson D, Van Allen EM, Wu YM, Schultz N, Lonigro RJ, Mosquera JM, et al. Integrative clinical genomics of advanced prostate cancer. *Cell.* 2015;161(5):1215-28.

24. Abida W, Cyrta J, Heller G, Prandi D, Armenia J, Coleman I, et al. Genomic correlates of clinical outcome in advanced prostate cancer. *Proceedings of the National Academy of Sciences of the United States of America.* 2019;116(23):11428-36.

25. Hofland J, Zandee WT, and de Herder WW. Role of biomarker tests for diagnosis of neuroendocrine tumours. *Nature reviews Endocrinology.* 2018;14(11):656-69.

26. Beltran H, Prandi D, Mosquera JM, Benelli M, Puca L, Cyrta J, et al. Divergent clonal evolution of castration-resistant neuroendocrine prostate cancer. *Nature medicine.* 2016;22(3):298-305.

27. Li P, Li M, Lindberg MR, Kennett MJ, Xiong N, and Wang Y. PAD4 is essential for antibacterial innate immunity mediated by neutrophil extracellular traps. *The Journal of experimental medicine.* 2010;207(9):1853-62.

28. Zhao S, Chuh KN, Zhang B, Dul BE, Thompson RE, Farrelly LA, et al. Histone H3Q5 serotonylation stabilizes H3K4 methylation and potentiates its readout.

Proceedings of the National Academy of Sciences of the United States of America. 2021;118(6).

29. Zhang Y, and Wang Y. The dual roles of serotonin in antitumor immunity. *Pharmacological research.* 2024;205:107255.

30. Zheng Q, Osunsade A, and David Y. Protein arginine deiminase 4 antagonizes methylglyoxal-induced histone glycation. *Nat Commun.* 2020;11(1):3241.

31. Wang L, Song G, Zhang X, Feng T, Pan J, Chen W, et al. PADI2-Mediated Citrullination Promotes Prostate Cancer Progression. *Cancer research.* 2017;77(21):5755-68.

32. Bi J, Khan A, Tang J, Armando AM, Wu S, Zhang W, et al. Targeting glioblastoma signaling and metabolism with a re-purposed brain-penetrant drug. *Cell reports.* 2021;37(5):109957.

33. Zhu P, Lu T, Chen Z, Liu B, Fan D, Li C, et al. 5-hydroxytryptamine produced by enteric serotonergic neurons initiates colorectal cancer stem cell self-renewal and tumorigenesis. *Neuron.* 2022;110(14):2268-82.e4.

34. Streubel G, Watson A, Jammula SG, Scelfo A, Fitzpatrick DJ, Oliviero G, et al. The H3K36me2 Methyltransferase Nsd1 Demarcates PRC2-Mediated H3K27me2 and H3K27me3 Domains in Embryonic Stem Cells. *Mol Cell.* 2018;70(2):371-9 e5.

35. Ferrari KJ, Scelfo A, Jammula S, Cuomo A, Barozzi I, Stützer A, et al. Polycomb-dependent H3K27me1 and H3K27me2 regulate active transcription and enhancer fidelity. *Molecular cell.* 2014;53(1):49-62.

36. Sardar D, Cheng YT, Woo J, Choi DJ, Lee ZF, Kwon W, et al. Induction of astrocytic Slc22a3 regulates sensory processing through histone serotonylation. *Science (New York, NY).* 2023;380(6650):eade0027.

37. Acharya NK, Nagele EP, Han M, Coretti NJ, DeMarshall C, Kosciuk MC, et al. Neuronal PAD4 expression and protein citrullination: possible role in production of autoantibodies associated with neurodegenerative disease. *Journal of autoimmunity.* 2012;38(4):369-80.

38. Chen L, Ji Y, Li A, Liu B, Shen K, Su R, et al. High-throughput drug screening identifies fluoxetine as a potential therapeutic agent for neuroendocrine prostate cancer. *Frontiers in oncology.* 2023;13:1085569.

39. Funazo T, Nomizo T, and Kim YH. Liver Metastasis Is Associated with Poor Progression-Free Survival in Patients with Non-Small Cell Lung Cancer Treated with Nivolumab. *Journal of thoracic oncology : official publication of the International Association for the Study of Lung Cancer.* 2017;12(9):e140-e1.

40. Cloyd JM, Ejaz A, Konda B, Makary MS, and Pawlik TM. Neuroendocrine liver metastases: a contemporary review of treatment strategies. *Hepatobiliary surgery and nutrition.* 2020;9(4):440-51.

Figures and figure legends

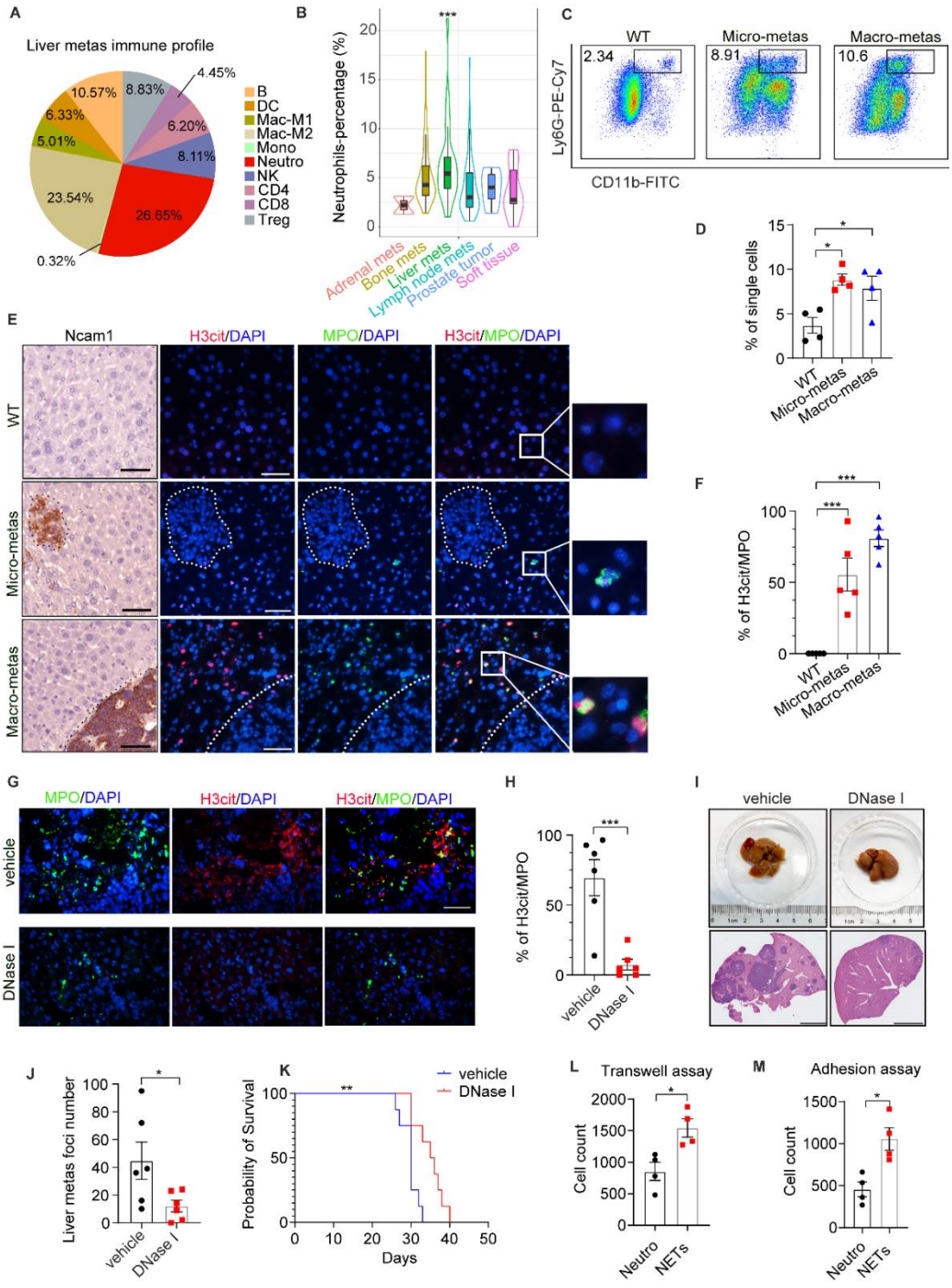

Figure 1. Neutrophils infiltration and NETs are detected in NEPC liver metastasis.

(A) Immune cell profiles of liver metastasis based on SU2C PCa dataset (n = 26).

(B) Neutrophil is the most enriched immune cell component in liver metastasis based on SU2C dataset (Adrenal mets, n = 2; Bone mets, n = 82; Liver mets, n = 26; Lymph

754 node mets, n = 79; Prostate tumor, n = 5; Soft tissue, n = 14). Data were mean ± SEM,
755 ***P < 0.001 was assessed using One-way ANOVA followed by the Dunnett's test.
756 **(C-D)** Flow cytometric plots **(C)** and quantification **(D)** on $CD11b^{+}Ly6G^{+}$ neutrophils
757 in livers (n = 4 mice).
758 **(E-F)** Immunohistochemical (IHC), immunofluorescence (IF) staining **(E)** and
759 quantification **(F)** for NETs in liver (n = 5 mice). Scale bar = 50 μm.
760 **(G-H)** IF staining **(G)** and quantification **(H)** on NETs ($H3cit^{+}$) in MPO-positive
761 neutrophils in livers of vehicle and DNase-I-treated NEPC-tumor-bearing mice (n = 6
762 mice). Scale bar = 50 μm.
763 **(I-J)** Images **(I)** of livers from vehicle and DNase-I treated NEPC-tumor-bearing mice.
764 H&E images **(I**, scale bars = 4 mm**)** and quantification **(J)** on liver metastases in
765 $Rb1^{\Delta/\Delta}Trp53^{\Delta/\Delta}$ organoid-inoculated mice via intravenous injection upon vehicle or
766 DNase-I treatment (n = 6 mice).
767 **(K)** The survival curves of vehicle and DNase-I treated NEPC-tumor-bearing mice (n
768 = 8 mice). Data were analyzed by Log-rank test. **P < 0.01.
769 **(L)** Quantification of migrated $Rb1^{\Delta/\Delta}Trp53^{\Delta/\Delta}$ PCa cells in Boyden chambers recruited
770 by murine primary neutrophils (neutro) or NETs (n = 4 biological replicates).
771 **(M)** Quantification of $Rb1^{\Delta/\Delta}Trp53^{\Delta/\Delta}$ PCa cells adhered by murine primary neutrophils
772 or NETs (n = 4 biological replicates).
773 For statistics in **(H), (J), (L)** and **(M)**, two-tailed student's *t*-tests were applied, and in
774 **(D)** and **(F),** the One-way ANOVA test was used followed by Turkey's test. Data were
775 shown as mean ± SEM, *P < 0.05 and ***P < 0.001.

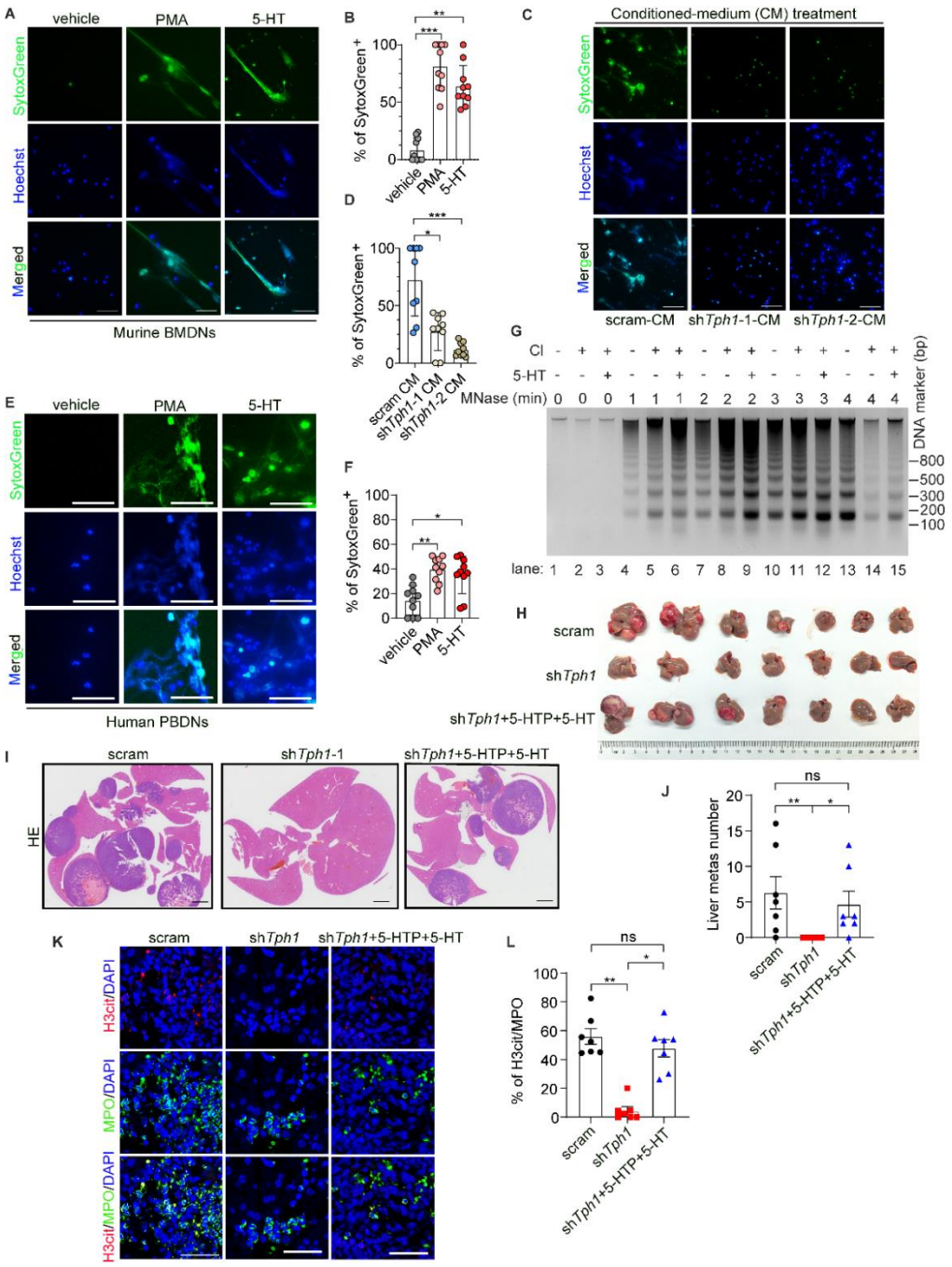

Figure 2. NEPC-derived-5-HT potentiates NETs formation and liver metastasis.

(A-B) IF staining images **(A)** and quantification results **(B)** showing NETs formation of murine bone-marrow-derived neutrophils (murine BMDNs) in response to 5-HT and vehicle control (n = 10 biological replicates). Scale bars = 50 μm. PMA induces NETs formation and serves as a positive control.

(C-D) IF staining images **(C)** and quantification results **(D)** showing NETs formation

of murine BMDNs upon the treatment of conditioned-media collected from scramble and sh*Tph1*-infected $Rb1^{\Delta/\Delta}Trp53^{\Delta/\Delta}$ organoids (n = 9 biological replicates). Scale bars = 50 μm.

(E-F) IF images **(E)** and quantification **(F)** on NETs formation capacity of human peripheral blood-derived neutrophils (PBDNs) upon 5-HT and vehicle control (n = 10 biological replicates). Scale bars = 50 μm.

(G) MNase digestion assay showing that addition of 5-HT induces decondensed NETs chromatin in HL-60 granulocytes compared to calcium ionophore treatment.

(H-J) In vivo experiments demonstrating a reduction of liver metastatic burden **(H)** in sh*Tph1*-infected as compared to scramble shRNA, and a regained liver metastatic burden in 5-HTP-treated-sh*Tph1*-infected $Rb1^{\Delta/\Delta}Trp53^{\Delta/\Delta}$ organoid-implanted mice via intravenous injection (n = 7 mice, each group). H&E staining **(I)** and quantification data validate significantly decreased liver metastatic foci numbers in *Tph1*-knockdown $Rb1^{\Delta/\Delta}Trp53^{\Delta/\Delta}$ organoid-inoculated mice and regained liver metastatic foci numbers in 5-HTP-treated mice **(J)**. Scale bars = 2 mm.

(K-L) IF images on liver sections **(K)** and quantification results **(L)** revealing a significant decline in NETs formation in *Tph1*-knockdown $Rb1^{\Delta/\Delta}Trp53^{\Delta/\Delta}$ organoid-inoculated mice (n = 7 mice, each group).

For **B, D, F, and L,** data were assessed using Kruskal-Wallis tests followed by Dunnett's tests. For **J**, data were analyzed using the One-way ANOVA followed by the Tukey's test. Data were mean ± SEM, *P < 0.05, **P < 0.01, ***P < 0.001. ns = no significance.

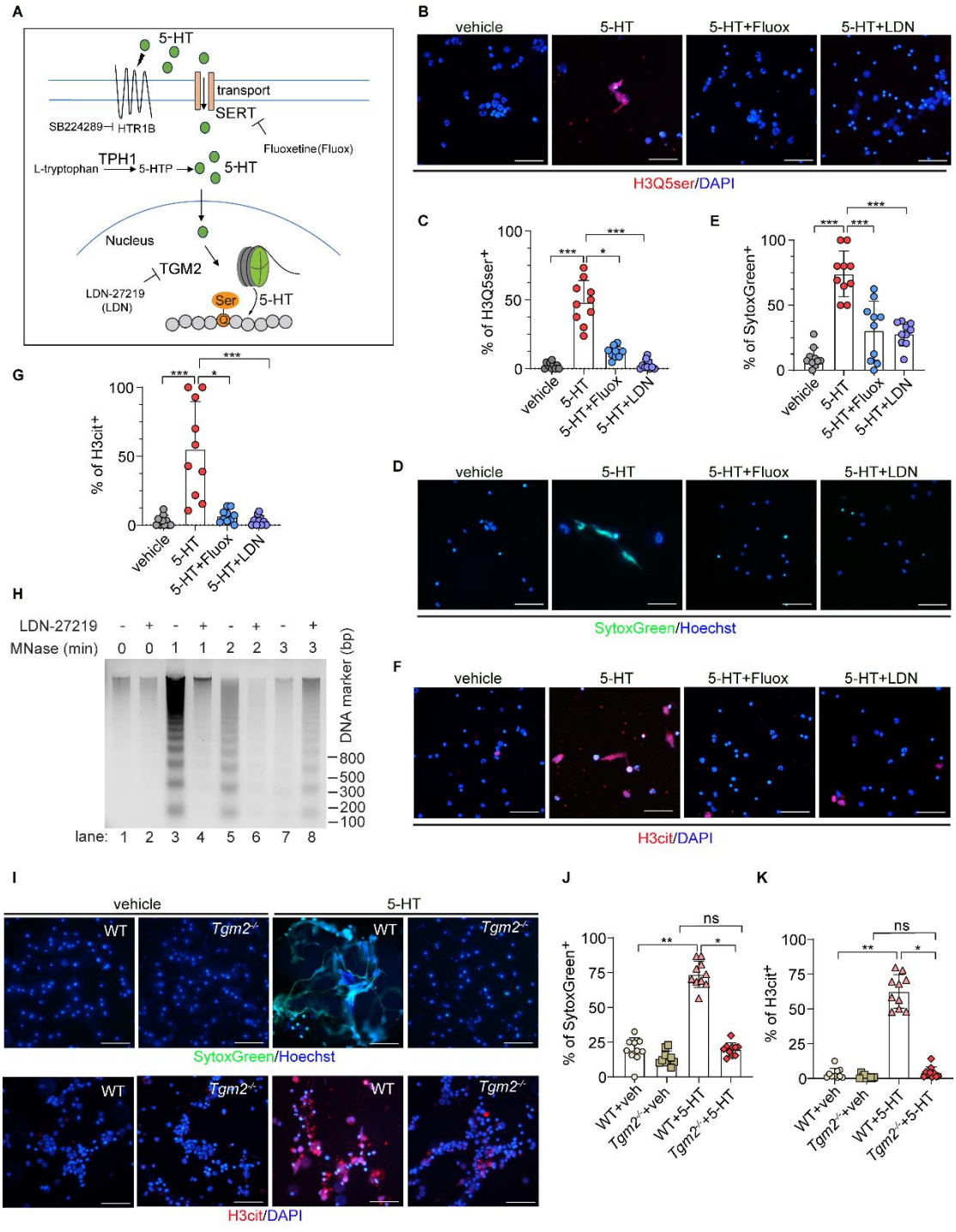

Figure 3. 5-HT induces histone serotonylation in neutrophils during NETs formation.

(A) A schematic chart showing the 5-HT-activated 5-HT/HTR signaling, SERT-mediated 5-HT intake, the TPH1-catalyzed 5-HT-biosynthesis, and the TGM2-catalyzed H3Q5ser.

(B-C) IF staining images **(B)** and quantification results **(C)** demonstrate that 5-HT addition promotes H3Q5ser modification in murine BMDNs, and SERT inhibitor fluoxetine (Fluox) and TGM2 inhibitor LDN-27219 (LDN) compromise 5-HT-induced H3Q5Ser (n = 10 biological replicates). Scale bars = 50 μm.

(D-G) IF staining results and quantification data reveal that fluoxetine and LDN-27219 abrogate 5-HT-induced NETs formation, as reflected by SytoxGreen **(D** and **E)** and H3cit **(F** and **G)** signals (n = 10 biological replicates per experiment). Scale bars = 50 μm.

(H) The MNase digestion assay showing that LDN-27219-treatment of HL-60 granulocytes leads to a delayed chromatin decondensation than vehicle controlment upon the stimulation of calcium ionophore.

(I-K) The *Tgm2*$^{-/-}$ mice-derived BMDNs showing significantly reduced NETs formation upon 5-HT stimulation, as exemplified by reduced SytoxGreen **(I** and **J)** and H3cit **(I** and **K)** signals, comparing to WT mice-derived BMDNs (n = 10 biological replicates per experiment). Scale bars = 50 μm.

For statistics in **C, G, J and K**, the Kruskal-Wallis tests were performed followed by Dunnett's tests. Data in **(E)** were assessed using the One-way ANOVA followed by the Tukey's test. Data were mean ± SEM, *P < 0.05, **P < 0.01 and ***P < 0.001. ns = no significance.

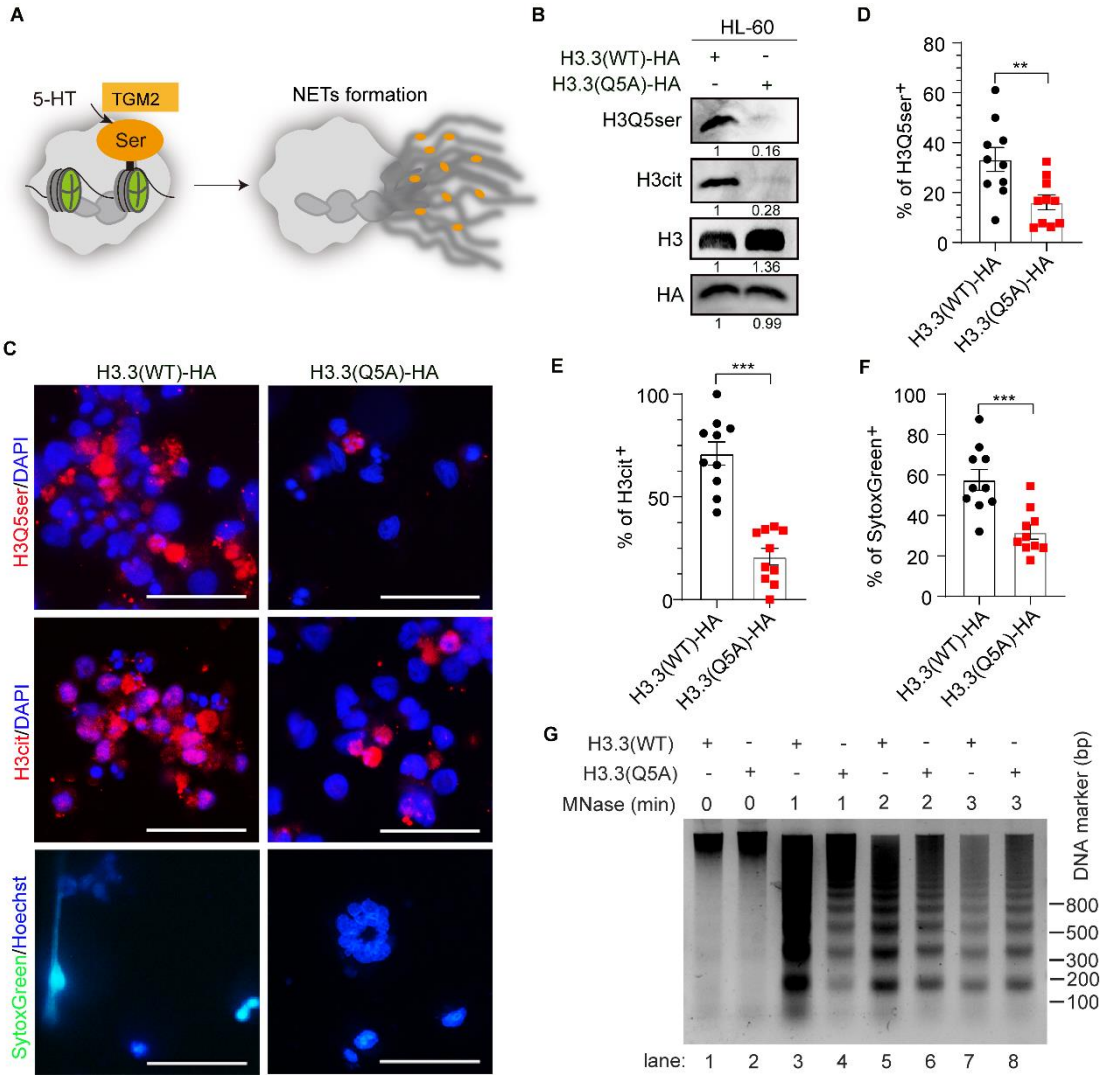

Figure 4. H3Q5Ser modification promotes NETs formation.

(A) A schematic diagram showing that 5-HT-mediated histone serotonylation promotes a decondensed chromatin state and facilitates NETs formation.

(B) Immunoblotting results demonstrate reduced levels of H3Q5Ser and H3Cit modifications in H3.3(Q5A) mutant as compared to H3.3-WT-transfected HL-60 granulocytes.

(C-F) IF staining images **(C)** and quantification data **(D-F)** showing reductions in H3Q5ser **(D)** and NETs formation in H3.3(Q5A) mutant-transfected HL-60 granulocytes cells, as reflected by decreased H3cit **(E)** and SytoxGreen **(F)** signals (n

= 10 biological replicates per experiment). In C, Scale bars = 50 μm.

(G) The MNase assay data reveal that chromatin in H3.3(Q5A)-transfected HL-60 granulocytes is less accessible than that in H3.3(WT)-transfected cells in response to calcium ionophore induction.

For statistics in **(D), (E) and (F)**, two-tailed student's *t*-tests were used and data were mean ± SEM, **P < 0.01 and ***P < 0.001.

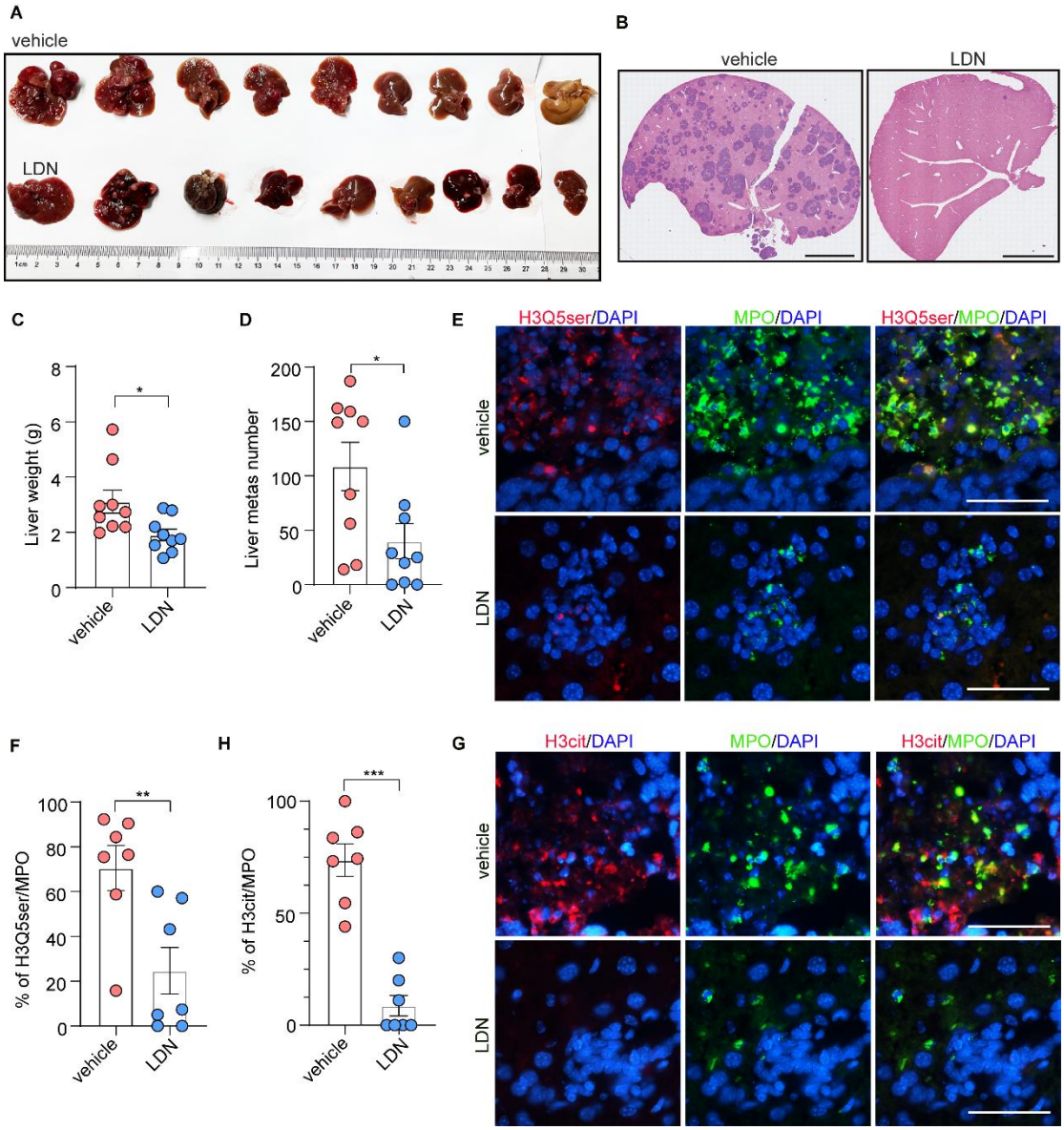

Figure 5. TGM2 inhibition abrogates NETs formation and liver metastasis in NEPC mouse models.

(A) TGM2 inhibitor LDN-27219 suppresses liver metastatic burden in *Rb1*$^{\Delta/\Delta}$*Trp53*$^{\Delta/\Delta}$-inoculated mice via intravenous injection (n = 9 mice, each group).

(B) H&E staining assay showing reduced liver metastatic foci in response to the treatment of LDN-27219. Scale bars = 4 mm.

(C-D) Quantifications on liver weights **(C)** and liver metastatic foci numbers **(D)** in *Rb1*$^{\Delta/\Delta}$*Trp53*$^{\Delta/\Delta}$-inoculated mice upon the treatment of vehicle and LDN-27219 (n = 9

mice, each group).

(E-F) IF staining images **(E)** and quantification results **(F)** showing decreased histone serotonylation (H3Q5ser^{+}) in hepatic neutrophil (MPO^{+}) in *Rb1*$^{\Delta/\Delta}$*Trp53*$^{\Delta/\Delta}$-inoculated mice upon the treatment of vehicle and LDN-27219 (n = 7 biological replicates). Scale bars = 50 μm.

(G-H) IF images **(G)** and quantifications **(H)** on neutrophil (MPO^{+})-derived NETs (H3cit) in *Rb1*$^{\Delta/\Delta}$*Trp53*$^{\Delta/\Delta}$-inoculated mice in response to vehicle and LDN-27219 (n = 7 biological replicates). Scale bars = 50 μm.

For **(C), (D), (F)** and (**H)**, the Mann-Whitney tests were applied and data were shown as mean ± SEM, *P < 0.05, **P < 0.01 and ***P < 0.001.

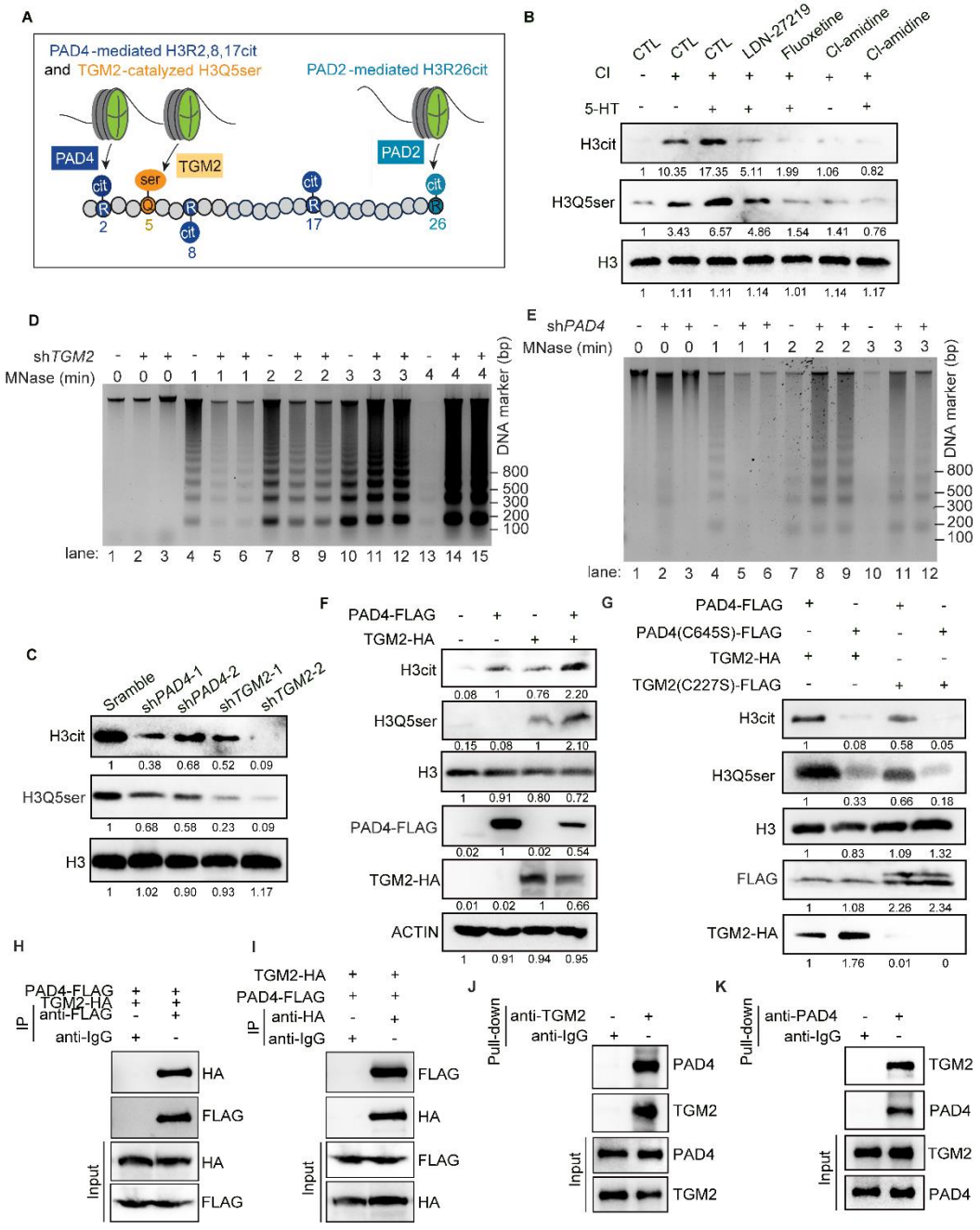

875

876 **Figure 6. TGM2 collaborates with PAD4 to coordinate histone serotonylation and**

877 **citrullination.**

878 **(A)** A schematic diagram showing proximal locations of TGM2-catalyzed H3Q5ser and

879 PAD4-mediated H3R2,8,17cit and PAD2-promoted H3R26cit on Histone H3.

880 **(B)** Immunoblotting assays demonstrate increased H3cit and H3Q5ser levels in HL-60-

881 derived granulocytes upon 5-HT stimulation.

(C) Immunoblotting data reveal reductions in H3cit and H3Q5ser modifications in either sh*PAD4* or sh*TGM2*-HL-60-cells compared to scramble shRNA-transfected cells. **(D-E)** The MNase assay data demonstrate that knockdown of either *TGM2* **(D)** or *PAD4* **(E)** in HL60 cells attenuates calcium ionophore-induced chromatin decondensation. **(F)** Dual expression of HA-tagged TGM2 and Flag-tagged PAD4 in HEK-293T cells showing elevated levels of both H3cit and H3Q5ser modifications. **(G)** Expression of enzyme-dead mutant of TGM2-C277S and PAD4-C645S in HEK-293T cells abrogates their synergistic effect in enhancing H3cit and H3Q5ser depositions. **(H-I)** Co-immunoprecipitation (co-IP) assay shows an exogenous interaction between TGM2 and PAD4 by IP Flag-tagged PAD4 **(H)** and HA-tagged TGM2 **(I)** in HEK-293T cells. **(J-K)** Pulldown assay demonstrates the protein-protein association between TGM2 and PAD4 *in vitro*.

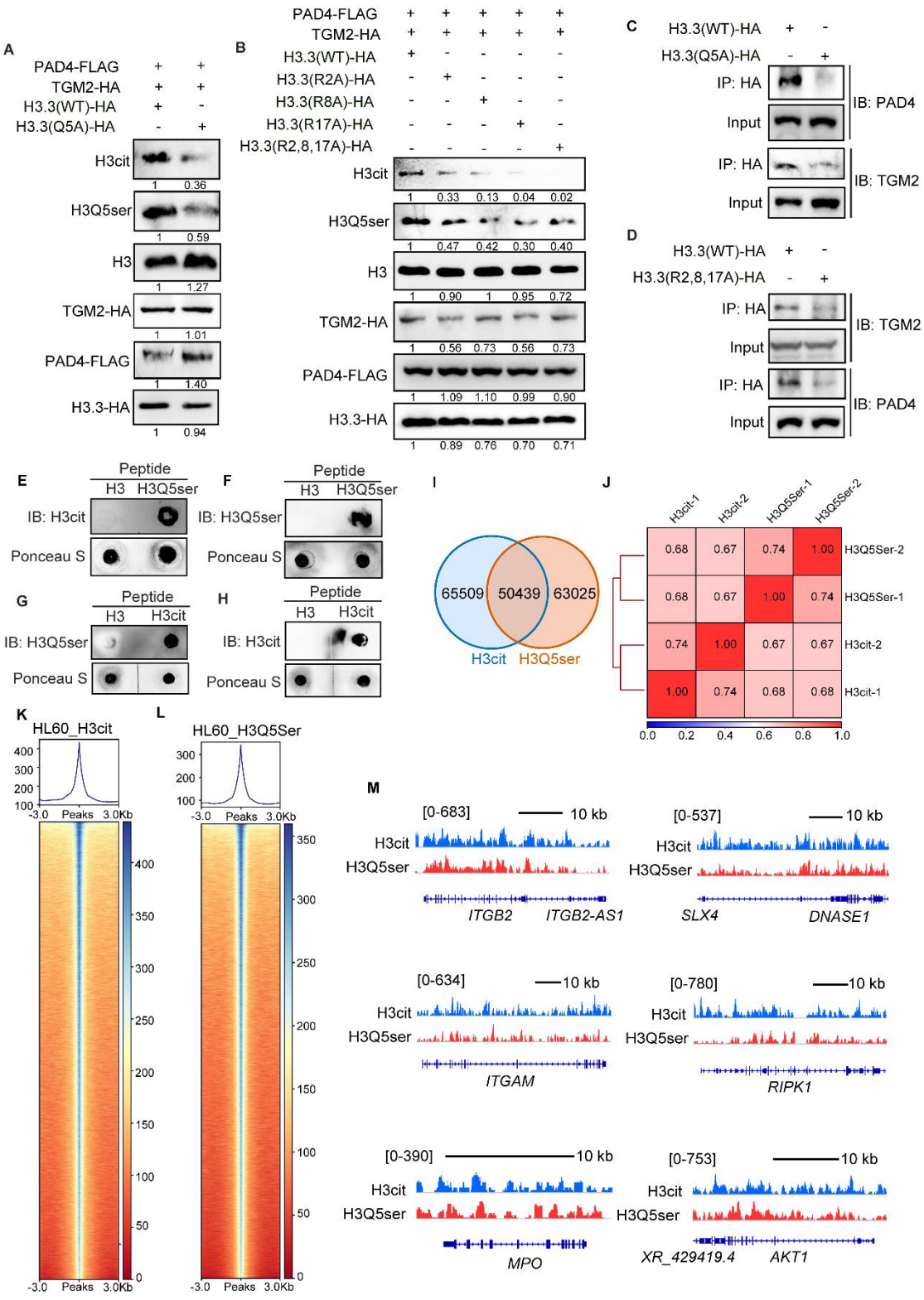

Figure 7. H3Q5ser and H3cit are mutually enhanced and share chromatin occupancy on a genome-wide scale.

(A) Immunoblotting assay demonstrates that the H3.3(Q5A) mutant leads to deficient

H3Q5ser modification and a reduced H3cit level.

(B) Immunoblotting data show that either H3.3(R2A), H3.3(R8A), H3.3(R17A) mutants alone or in combination H3.3(R2,8,17A) result in deficient H3cit modification and a repressed H3Q5ser level.

(C-D) Mutant H3.3(Q5A) **(C)** or H3.3(R2,8,17A) **(D)** attenuates the recruitment of each other's epigenetic writer, as exemplified by deficient binding of either PAD4 **(C)** or TGM2 **(D)** to histone H3.

(E-F) In vitro catalytic assay showing that H3Q5ser-modified peptides enhance PAD4-mediated H3cit compared to unmodified H3 peptide control.

(G-H) In vitro catalytic assay revealing that H3cit-modified peptides promote TGM2-mediated H3Q5ser compared to unmodified H3 peptide control.

(I) Venn diagrams show the overlapped H3cit and H3Q5ser peaks in HL-60 granulocytes from CUT&Tag sequencing data (2 independent experiments).

(J) Heatmap showing the genome-wide Spearman's correlation between the H3Q5ser and H3cit modifications (2 independent experiments).

(K-L) Heatmaps of H3cit **(K)** and H3Q5ser **(L)** peaks are showed on a genome-wide scale in HL-60 granulocytes (2 independent experiments).

(M) CUT&Tag profiles of co-occupied NETs related genes including *ITGB2*, *DNASE1*, *ITGAM*, *RIPK1*, *MPO*, and *AKT1* of H3cit and H3Q5ser modifications in HL-60 granulocytes (2 independent experiments).

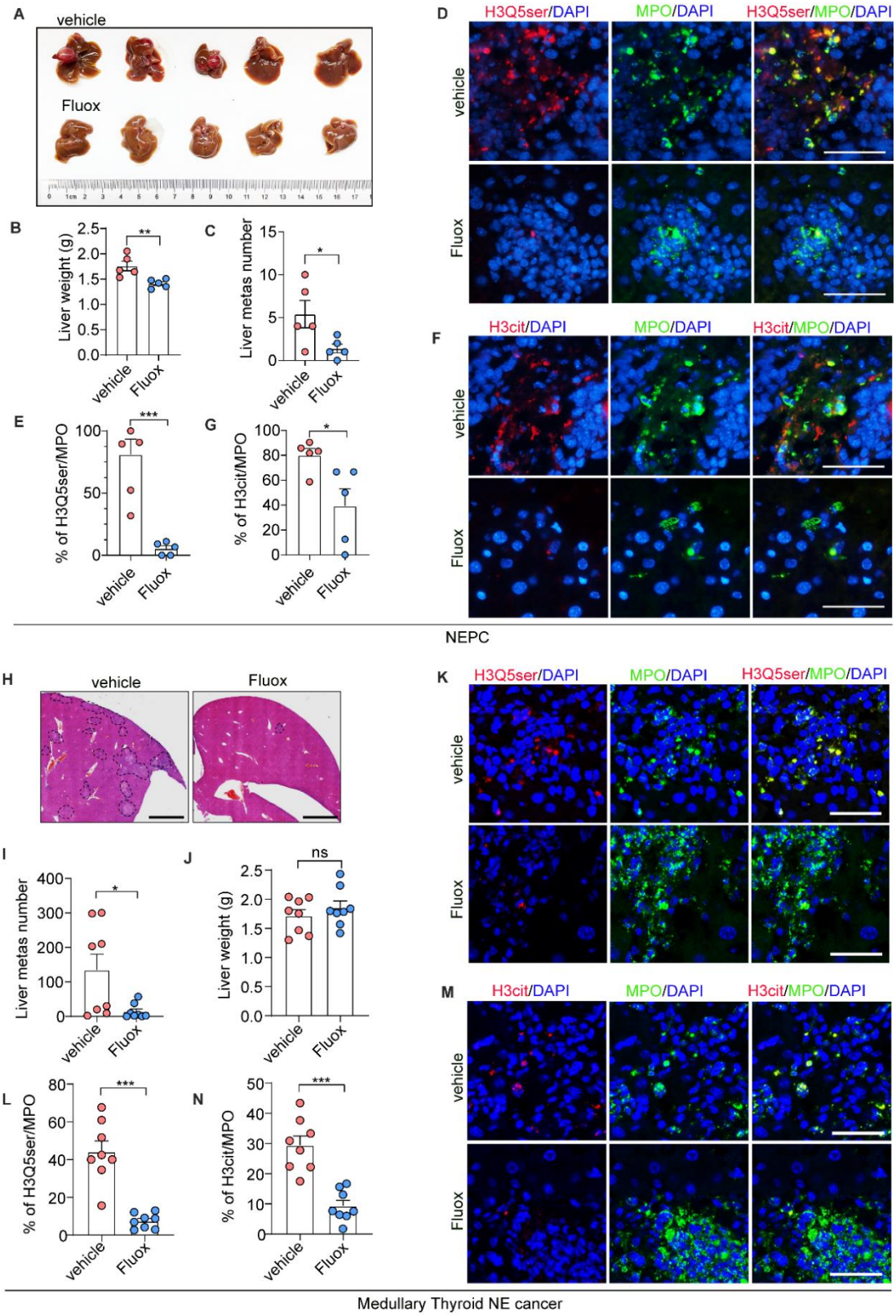

Figure 8. SERT inhibitor fluoxetine represses NETs formation and liver metastasis in NE-cancers.

(A-C) SERT inhibitor fluoxetine suppresses liver metastasis **(A)** in *Rb1*$^{\Delta/\Delta}$*Trp53*$^{\Delta/\Delta}$-

intravenously inoculated mice, as exemplified by decreased liver weights **(B)** and metastasis foci numbers **(C)**, comparing to vehicle-treated ones (n = 5 mice, each group). **(D-E)** IF staining images **(D)** and quantification results **(E)** showing decreased histone serotonylation (H3Q5ser^{+}) in hepatic neutrophils (MPO^{+}) in *Rb1*$^{\Delta/\Delta}$*Trp53*$^{\Delta/\Delta}$-inoculated mice upon the treatment of fluoxetine as compared to vehicle (n = 5 mice, each group). Scale bars = 1.5 mm.

(F-G) IF images **(F)** and quantifications **(G)** on neutrophil (MPO^{+})-derived NETs (H3Cit) in *Rb1*$^{\Delta/\Delta}$*Trp53*$^{\Delta/\Delta}$-inoculated mice in response to vehicle and fluoxetine (n = 5 mice, each group). Scale bars = 50 μm.

(H-J) H&E staining images **(H)** and quantification results showing decreased metastasis foci numbers (**I**) in TT-cells-inoculated mice via intravenous injection upon the treatment of fluoxetine, comparing to vehicle-treated counterparts (n = 8 mice, each group). Scale bars = 1 mm.

(K-L) IF staining images **(K)** and quantification results **(L)** showing decreased H3Q5ser^{+} in MPO^{+} in TT-inoculated mice upon the treatment of fluoxetine as compared to vehicle (n = 8 mice, each group). Scale bars = 50 μm.

(M-N) IF images **(M)** and quantifications on NETs (**N**) in TT-inoculated mice in response to vehicle and fluoxetine (n = 8 mice, each group). Scale bars = 50 μm.

For statistics in **(B), (C), (E), (J), (L) and (N)**, two-tailed student's *t*-tests were used and data were mean ± SEM, *P < 0.05, **P < 0.01, ***P < 0.001, and ns = no significance. For (**G**) and **(I)**, data were mean ± SEM, *P < 0.05 was assessed using Mann-Whitney tests.